Parallel interrogation of the chalcogenide-based micro-ring sensor array for photoacoustic tomography

Jingshun Pan
Sun Yat-sen University

Qiang Li
Sun Yat-sen University

Yaoming Feng
School of Electronics and Information Technology, Sun Yat-sen University

Ruifeng Zhong
Sun Yat-sen University

Zhihao Fu
Sun Yat-sen University

Shuixian Yang
Sun Yat-sen University

Weiyuan Sun
Sun Yat-sen University

Bin Zhang
Sun Yat-sen University

Qi Sui
Southern Marine Science and Engineering Guangdong Laboratory (Zhuhai)

Jun Chen
Sun Yat-sen University   https://orcid.org/0000-0001-7397-2714

Yuecheng Shen (✉ shenyuecheng@mail.sysu.edu.cn)
Sun Yat-sen University   https://orcid.org/0000-0003-1990-8142

Zhaohui Li
Sun Yat-sen University   https://orcid.org/0000-0002-6145-7843

Abstract

Photoacoustic tomography (PAT), also known as optoacoustic tomography, is an attractive imaging modality that provides optical contrast with acoustic resolutions. Recent progress in the applications of PAT largely relies on the development and employment of ultrasound sensor arrays with many elements. Although on-chip optical ultrasound sensors have been demonstrated with high sensitivity, large bandwidth, and small size, PAT with on-chip optical ultrasound sensor arrays is rarely reported. In this work, we demonstrated PAT with a chalcogenide-based micro-ring sensor array containing 15 elements, while each element supports a bandwidth of 175 MHz and a noise-equivalent pressure of 2.2 mPaHz$^{-1/2}$. Moreover, by synthesizing a digital optical frequency comb (DOFC), we further developed an effective means of parallel interrogation to this sensor array. As a proof of concept, parallel interrogation with only one light source and one photoreceiver was demonstrated for PAT with this sensor array, providing images of fast-moving objects, leaf veins, and live zebrafish. The superior performance of the chalcogenide-based micro-ring sensor array and the effectiveness of the DOFC-enabled parallel interrogation offer great prospects for advancing applications in PAT.

Introduction

Biomedical imaging serves as an effective tool in life science to explore the mystery in behaviors and recognitions of humans and animals. Among various biomedical imaging modalities, photoacoustic (PA) tomography (PAT), also known as optoacoustic tomography, is a hybrid imaging modality that combines optical excitation and ultrasonic detection [1, 2]. This marriage overcomes the disadvantages of low contrast in ultrasonic imaging and shallow depth in optical imaging, making PAT a promising tool for deep-tissue high-resolution structural and functional imaging in vivo. Currently, PAT has been demonstrated with great success with many preclinical and clinical applications, such as whole-body imaging for small animals [3], functional imaging for mouse and human brains [4, 5], and human breast imaging for cancer screening [6, 7]. In these demonstrations, sensor arrays that contain many commercial piezo-electric ultrasound sensors were generally adopted. However, these bulk sensors suffer from limited acceptance angle, sensitivity, and frequency bandwidth, degrading imaging quality and causing reconstruction artifacts. Moreover, high framerate three-dimensional PAT requires a large number of elements, leading to huge system complexity with complicated electrical interconnects. To overcome this challenge, optical ultrasound sensors with a small footprint, large acceptance angle, high sensitivity, and broad frequency bandwidth are becoming promising substitutes [8].

A variety of optical ultrasound sensors have been proposed to detect pressure-induced optical changes, which reflect the amplitude of the acoustic waves [8]. Thanks to the abundant means to address optical signals, optical ultrasound sensors have now shown superior performances in different aspects with interferometric methods. For example, fiber-optic interferometers can serve as high-performance ultrasound sensors, bringing excellent flexibility to PAT by enabling different imaging configurations [9–11]. Moreover, fiber tips with engineered micro-resonators, such as in-fiber Bragg grating [12] and Fabry-Perot structure [13–15], can also be made as sensitive ultrasound probes to image vascular structure in

endoscopy [16]. Moreover, by exploiting the platform of silicon photonics, miniaturized ultrasound sensors based on Bragg grating can be made with a small footprint [17–19], even down to the size of a sub-micrometer [20, 21]. Alternatively, micro-ring resonators have the advantages of high-quality factor, miniaturized form factor, and optical transparency [22–26]. To date, optical ultrasound sensors that employ either polymer-based [22, 23] or silicon-based [27] micro-rings can achieve a high-quality factor up to 10^5 with a small footprint [28, 29], an ultrabroad frequency bandwidth up to 350 MHz [30], high sensitivity with a noise-equivalent pressure (NEP) down to 1.3 mPaHz$^{-1/2}$ [27], and a wide acceptance angle over ± 30 degrees (3-dB line) [25]. Using micro-ring ultrasound sensors, PAT with laser-scanning endoscopy on tube phantoms [31] and microscopy on single cells [32], mouse ears [29], and mouse brains [33] have been demonstrated. Recently, three-dimensional PAT for a variety of biological tissue with an imaging depth up to 8 mm has also been reported [34].

Despite these accomplishments, these demonstrations on PAT mainly employ only a single element, which means tomographic images require a time-consuming scanning process to form. In contrast, PAT equipped with an ultrasound sensor array with many elements can facilitate imaging speed and improve imaging quality. Etalon sensors based on Fabry-Perot cavities are naturally two-dimensional sensor arrays [35, 36]. However, parallel interrogation requires photodetector arrays with increased electrical complexity and suffers from considerable crosstalk. Similarly, fiber-optic detector arrays also require a rather complicated imaging system [10, 37, 38]. Back in 2008, Maxwell et al. reported the first integrated on-chip sensor array with four micro-rings [22]. The relatively low-quality factor of the micro-rings fabricated at that time causes spectrum overlapping between adjacent resonant frequencies, making each element in the array difficult to function simultaneously. Recently, a one-dimensional sensor array containing ten micro-rings was reported with a well-separated spectrum for adjacent resonant frequencies [27]. However, as this system had only one laser and one photoreceiver, only one micro-ring sensor can work at a time. It is expected that parallel interrogation could be realized by the means of wavelength division multiplexing [37], but it either requires a sufficient number of source-detector pairs [27] or a frequency swept source [38]. Simultaneous multi-channel ultrasonic detection of up to four elements was reported via phase-modulated pulse [39], but it still requires one photoreceiver per detecting channel, which increases system complexity. Thus, there is an urgent need to not only fabricate compact and integrated on-chip optical ultrasound sensor arrays with a large number of elements but also develop efficient means to interrogate them in parallel.

To fill this blank, we reported a micro-ring sensor array in this work, which contains 15 high-quality micro-rings coupled to a bus straight waveguide. These structures were made of chalcogenide materials with large elastic-optical coefficients and low Young's modulus. Specifically, these micro-rings were characterized with high-quality factors ranging from 5×10^5 to 7×10^5, a frequency bandwidth up to 175 MHz (-6 dB), an NEP down to 2.2 mPaHz$^{-1/2}$ or 7.1 Pa within a 20-MHz range, an acceptance angle of ± 30 degrees (-3 dB), and a small footprint of $0.85 \times 40 \times 40$ μm^3. To realize simultaneous operation, these micro-rings were delicately tuned with slightly different resonant frequencies. Assisted by a delicately synthesized digital optical frequency comb (DOFC), we further developed an effective means of parallel

interrogation to the sensor array, which only requires one laser source and one photoreceiver in the system to perform PAT. As schematically shown in Fig. 1, the DOFC passes through the sensor array and acquires the information of the laser-induced PA signals, enabling one-time measurement for the transmission spectrum using only a single photoreceiver. The knowledge of the complete transmission spectrum allows the determination of the PA signals received by all micro-rings simultaneously, allowing the formation of the images in a single-shot measurement. Equipped with the chalcogenide-based micro-ring sensor array and the means of parallel interrogation, we experimentally demonstrated PAT on fast-moving objects like a laser-scanning hot spot and a water-pulled microsphere. We further performed PAT with broad beam illumination on leaf veins buried inside thick tissue-mimicking phantom and live zebrafish at various growth stages. These results indicate that the chalcogenide-based micro-ring sensor array, together with the DOFC-enabled parallel interrogation, offers great prospects for clinical applications in PAT.

Methods

Structure of the sensor array. The main parts of the sensor array are the micro-ring sensors and the bus waveguide. The scanning electron micrographs of a micro-ring sensor and a bus waveguide are shown in Figs. 2(a) and 2(b), respectively. Each micro-ring sensor has a diameter of 40 µm, a cross-sectional height of 850 nm, and a width of 2.4 µm. They are also separated with a center-to-center distance of 400 µm and each of them occupies an effective area of about $0.85 \times 40 \times 40$ µm^3. Note that the resonant frequency of each micro-ring sensor was tuned to be slightly different through photosensitive effect, which is detailed in Supplementary Note 3. The width and the height of the bus waveguide are 650 nm and 850 nm, respectively. Both the micro-ring sensor and the bus waveguide were fabricated using chalcogenide material with a composition of $Ge_{25}Sb_{10}S_{65}$, exhibiting a refractive index of 2.33 around 1,550 nm. This material has a good photoelastic property with Young's modulus of 31.9 GPa, leading to a good sensitivity to ultrasound. These nano-fabricated structures sit on top of a silica (SiO_2) substrate and are covered with a 3-µm-thick polydimethylsiloxane (PDMS) cladding. This cladding is important in protecting micro-rings in an aqueous environment. No other micro/nanostructures are required to enhance the performance of the sensor array. By using the finite element method (COMSOL Multiphysics 5.6), Figs. 2(c) and (d) show the numerically simulated intensity distribution of the propagating modes inside the micro-ring sensor and the waveguide, respectively, exhibiting good mode confinement. For practical considerations, we fabricated many micro-ring sensor arrays with different parameters on one chip, as shown in the microscope image in Fig. 2(e). After examining the performance, the part that only contains one sensor array was cleaved and encapsulated, occupying a small footprint of about 6 mm × 2 mm. As a comparison, a nickel coin with a 2-cm diameter was placed underneath, as shown in Fig. 2(f). In particular, the end of the bus waveguide, which is enclosed in a red box in Fig. 2(f), was attached to a single-mode optical fiber, with an enlarged view shown in Fig. 2(g).

The fabrication process of the sensor array. We firstly prepared an 850-nm-thick $Ge_{25}Sb_{10}S_{65}$ film and deposited it on a silicon wafer with a 3-µm-thick oxidized layer using the thermal evaporation technique.

To prevent oxidation of the chalcogenide film during subsequent processes, 2-nm-thick alumina oxide was deposited through atomic layer deposition (Kemicro, ALD-100A). After spin-coating a layer of positive photoresist (Allresist, ARP6200) onto the chalcogenide film, electron beam lithography (Raith, EBPG5000+) was employed to write the pattern, i.e., the micro-rings and coupling waveguides. The pattern was then transferred onto the chalcogenide film by using reactive ion etching (Oxford Instrument, PlasmaPro 100RIE). The residual photoresist was removed through appropriate treatment with oxygen plasma, forming the basic structure of the on-chip micro-ring sensor array. In order to improve the durability of the chip, we spin-coated 4-μm-thick PDMS (Dow-corning, GZJ-184) to the entire chip for encapsulation. After completing the thermal curing of the PDMS film (curing agent ratio: 23%), the sensor array can now be exposed to the normal environment.

Experimental setup for PAT using the sensor array. The experimental setup of employing the micro-ring sensor array for PAT is shown in Fig. 3(a). A continuous-wave narrow-linewidth tunable laser (Keysight, 8164B, 10-kHz linewidth, 1,550 nm) was chosen as the optical source for the sensor array. Its frequency was tuned to be close to the resonant frequencies of these micro-rings. The output light of the laser was divided into a signal beam and a local oscillator through a polarization-maintaining fiber coupler (Thorlabs, PNH1550R5A1). The signal beam interacted with the sensor array to probe the information carried by the ultrasonic wave. In this work, we employed a DOFC to realize parallel interrogation to the sensor array, which has the advantages of stability, flexibility, and tunability. It is worth noting that the DOFC has been demonstrated previously for ultrafine spectral measurement (0.01 pm resolution) [40] and low-frequency ultrasound detection (165 kHz) [41]. For a fiber-based resonator, a similar comb structure was also created optically with pulsed light and two fiber Bragg gratings for ultrasonic detection [12]. In this work, the generation of the DOFC started with a digital signal with a multi-carrier bandwidth of 40 GHz and a sequence length of 1,536, which was synthesized through the orthogonal frequency division multiplexing method. The digital signal was then fed into an arbitrary waveform generator (Keysight, M8195A) with a sampling frequency of 60 GHz. In this condition, the corresponding spacing of the subcarrier, i.e., the comb tooth spacing, is 39.0625 MHz (60 GHz/1536). The signal was then amplified and periodically sent to an intensity modulator (Xblue, MXER-LM-20). By setting the intensity modulator with a bias control at the node point, a carrier suppressed double-sideband modulated DOFC signal was generated with a bandwidth of about 40 GHz (320 pm @1550 nm). Detailed mathematical descriptions of the generation of the DOFC can be found in Supplementary Note 1. The DOFC then passed through the sensor array to probe PA signals. Having acquired the information from the sensor array, the DOFC was then post-amplified by an erbium-doped fiber amplifier (Amonics, AEDFA-PA-35-B-FA) and filtered by an optical tunable filter (Santec, OTF-350). Finally, the DOFC was combined with the local oscillator, which was subsequently measured by a coherent receiver (Finisar, CPRV122xA) and digitized by an oscilloscope (Lecroy, 10-36Zi-A). A digital signal processing unit performed Fourier transformation to the measured signal and reconstructed the transmission spectrum of the sensor array (also detailed in Supplementary Note 1). It is worth emphasizing that the employment of the DOFC allows the determination of the transmission spectrum in a one-time measurement, without the need for time-consuming frequency sweeping. In the measured transmission spectrum, the amount of resonant frequency shift reflects the

amplitude of the received PA signal. Taking 15 micro-rings as an example, Fig. 3(b) plots the measured transmission spectrum as a function of time in the null case. Notably, the resonant frequency of each micro-ring remains as a flat line, indicating a stable detecting environment due to the encapsulation of the sensor array. When the laser-induced ultrasound signal is present to modulate these micro-rings, Fig. 3(c) plots the measured transmission spectrum as a function of time. In this condition, the amount of resonant frequency shift for each micro-ring sensor faithfully represents the amplitude of the PA signal measured by each element. The time delay reflects the relative distance between the ultrasonic source and the micro-ring sensor. As a result, the reconstructed PA signal as a function of time for each micro-ring sensor is illustrated in Fig. 3(d).

Characterization of the micro-ring sensor. We first characterize the performance of the micro-ring sensor in an aqueous environment. As shown in Fig. 4(a), a point ultrasound source was generated by focusing pulsed light (Elforlight, SPOT-10-200-532, 2.6-ns pulse width) onto a 200-nm-thick golden thin film [27, 30]. The micro-ring sensor array was positioned 5 mm aside to measure the PA signal. A motorized linear translational stage was used to control the position of the sensor array. Both the thin film and the micro-ring sensor were immersed inside the water that serves as the coupling medium for the ultrasonic wave. For a single micro-ring sensor, the received PA signal as a function of time is plotted in Fig. 4(b), which can be treated as the impulse response of delta excitation. To remove unwanted signals due to multiple reflections between substrates, we enforced a time window to keep only the first arriving signals (highlighted in the red dashed box in Fig. 4(b)). Thus, the frequency response of the micro-ring sensor can be estimated by taking the Fourier transformation to the time-gated signal, which is plotted in Fig. 4(c). The central frequency locates around 60 MHz, and the − 6 dB bandwidth is estimated to be 175 MHz (the − 3 dB bandwidth is 120 MHz). We also quantified the acceptance angle of the micro-ring sensor by continuously scanning the position of the sensor, while keeping the position of the point ultrasound source. Figure 4(d) shows the amplitude map of the measured PA signal as a function of time and translational distance. By transforming time into frequency and position into acceptance angle, the frequency response of the micro-ring sensor as a function of the acceptance angle is shown in Fig. 4(e). Two white − 3 dB lines are also provided for visualization purposes. As we can see from the figure, a wide detection angle of about ± 30 degrees can be realized even up to 70-MHz bandwidth. Then, we followed the procedures described in Ref. [27] to characterize the sensitivity of the micro-ring sensor, with the assistance of a calibrated hydrophone (Precision Acoustics, NH0200, 20-MHz bandwidth). The noise amplitude spectral density was calculated when no ultrasound was present, which is provided in Fig. 4(f). By dividing the noise amplitude spectral density with respect to the sensitivity, Fig. 4(g) shows that the NEP spectral density is below 2.2 mPaHz$^{-1/2}$, leading to the measured NEP of 7.1 Pa within 20-MHz bandwidth. These values are comparable to those of the state-of-the-art optical ultrasound sensors [19, 27]. The detailed calculation process for obtaining these values can be found in Supplementary Note 2. In PAT, the imaging resolution is determined by the detecting bandwidth of the micro-ring sensor. This parameter was quantified by replacing the golden thin film in Fig. 4(a) with two horizontally placed carbon fibers (7−8 µm in diameter) buried inside the agar. The cross-section of the fiber was imaged to provide information on the point spread function of the imaging system. The micro-ring sensor was

linearly translated with a step size of 20 µm with a 2-mm range. Universal back-projection (UBP) [42] was employed to synthesize detected PA signals at each position and produce the image in Fig. 4(h), which contains two carbon fibers. One-dimensional profiles for quantifying both the lateral and axial resolutions are illustrated in Figs. 4(i) and (j), exhibiting full width at half maximum of about 80 and 24 µm, respectively. Note that the discrepancy along the two directions is because lateral resolution mainly depends on the center frequency while the axial resolution is primarily determined by the bandwidth [34].

Frequency tuning of the micro-ring sensor array. The micro-ring sensor array used in this work contains 15 micro-rings, serving as a linear array for PAT. Since slight deviations in terms of diameter of these micro-rings (10 nm) are inevitable due to the fabrication precision of electron beam lithography, the resonant frequencies of these micro-rings were randomly displayed at the beginning. To facilitate the demodulation process of the DOFC and enable parallel interrogation, ordering and equally spacing these resonant frequencies are critically important. This requirement can be fulfilled by exploiting the strong photosensitive effect of chalcogenide glasses [43, 44]. Experimentally, we used an optical fiber to illuminate each micro-ring sensor with 532-nm pulsed light. By controlling the illuminating intensity and time duration, the resonant frequency of the micro-ring sensor is reconfigurable with the desired amount. Illuminating light can be removed later after reconfiguring these resonant frequencies. Detailed operational procedures for rearranging the resonant frequencies of these micro-rings can be found in Supplementary Note 3. After the tuning process, it is shown in Fig. 5(a) that the resonant frequencies of these micro-ring sensors are now ordered with respect to their labeling and equally spaced. The average separation between adjacent resonance frequencies is about 1.66 GHz (0.02 nm @ 1550 nm), and these resonant frequencies occupy an overall spectrum range of 23.7 GHz (0.32 nm @ 1550 nm). As shown in Fig. 5(b), after frequency tuning, the quality factors of these micro-ring sensors were also quantified with good consistency, which fell within the range of 5 to 7×10^5. As a result, a typical transmission spectrum of the micro-ring sensor array is shown in Fig. 5(c), exhibiting 15 distinct and equally separated resonant dips within a frequency range of -11 ~ 12.7 GHz (with respect to the center of the DOFC).

Results

Experimental results on imaging fast-moving objects. We first implemented parallel interrogation to the sensor array on imaging fast-moving objects. In the first demonstration, a fast-moving hot spot was created by scanning a focused light pulse on a black tape through a two-axis galvo-mirror. The focused pulse light was generated by the same laser used for sensor characterization, which has a repetition rate of 10 kHz. The hot spot, which has a diameter of about 100 µm and an energy of 1 nJ, moved along a trajectory of an '8' shape. The DOFC enables parallel interrogation of the PA signals for all micro-ring sensors simultaneously, and UBP was employed to reconstruct the image for this linear array. Although the frame rate under this imaging scheme can be up to 10 kHz, we pick only eight representative images within a time window of 5 ms to reveal the moving trajectory of the created hot spot in Fig. 6(a). An outline of '8' is provided in white for visualization purposes.

Besides imaging a virtual hot spot, we also demonstrated imaging a physically presented polystyrene microsphere in motion. The microsphere has a diameter of 200 μm and was placed inside a plastic tube with a 500-μm inner diameter. The plastic tube was pumped with flowing water, pushing the microsphere to move downward. In this demonstration, a 532-nm Nd: YAG laser (Beamtech, Dawa 100) with a pulse width of 6.5 ns and a repetition rate of 20 Hz was employed to illuminate the region of interest. A ground glass diffuser (Thorlabs, DG10-120) expanded the pulsed light (1.4 mJ) with a fluence rate of about 19.7 mJ /cm^2 and an illumination spot with a 3-mm diameter. Images reconstructed at different time intervals are shown in Fig. 6(b), exhibiting good reliability in imaging moving objects using the micro-ring sensor array with parallel interrogation.

Experimental result on imaging biological samples (leaf vein and live zebrafish). We further applied the micro-ring sensor array with parallel interrogation on imaging biological samples with complex structures. To mitigate unwanted artifacts due to limited view, biological samples were mounted on a motorized rotational stage. The scanning step size was set to 1 degree during the experiment. The first biological sample to be imaged is a piece of leaf buried inside a 5-mm-thick tissue-mimicking phantom (transport mean free path ~ 1 mm^{-1} at 532 nm). The fluence rate on the surface of the phantom was about 7 mJ/cm^2 and the illumination area has a diameter of about 8 mm. Figure 7(a) shows the reconstructed image of the leaf using the micro-ring sensor array, showing clear vein structures along various directions. As a comparison, the reconstructed image using only one micro-ring is shown in Fig. 7(b). Notably, leaf veins in Fig. 7(a) exhibit a much better contrast than that in Fig. 7(b). In particular, enlarged images of the part enclosed in the white boxes of Figs. 7(a) and (b) are also shown in Figs. 7(c) and (d), respectively. To quantify the contrast-to-noise ratio (CNR) of these images, Fig. 7(e) plots the signal strength along the white dashed lines in Figs. 7(a) and (b). Here, CNR is defined as the ratio of the peak value and the standard deviation of the background (away from the center). The improvement in CNR by using the micro-ring array compared to a single micro-ring is about 5.51 dB, which is close to the theoretical enhancement due to the element number $\left(\sqrt{15}\right)$. These results confirm the superiority of the micro-ring sensor array over a single micro-ring sensor.

We also performed PAT for live zebrafish at the different growth stages, by using the DOFC-enabled parallel interrogation for the micro-ring sensor array. The zebrafish was firstly anesthetized using water with 0.016% tricaine and then moved to the imaging area. To minimize the movement of the live zebrafish, its abdomen was covered with 1% low-melting-point agar. All experiments using zebrafish were conducted under the auspices of animal ethics. The general breeding and handling of zebrafish were conducted following standard protocols from the Institutional Animal Care Committee of Sun Yat-sen University. As mentioned above, the fluence rate is about 7 mJ/cm^2, which is much lower than the American National Standards Institute (ANSI) safety limit. Details on the imaging setup of the animal experiment are provided in Supplementary Note 4. For a 3-month-old adult zebrafish, we imaged its head and tail in Figs. 7(f) and (g), respectively. We also performed whole-body imaging for smaller zebrafish that were 7 days and 20 days post-fertilization, and the reconstructed images are shown in Figs. 7(h) and (i), respectively. As we can see from the figure, both the outlines of the zebrafish and their organs like eye,

heart, trunk, yolk sac, dorsal aorta, cardinal vein, dorsal longitudinal anastomotic vessel, spinal column, dorsal fin, and anal fin can be identified. These imaging results demonstrate the feasibility of the micro-ring sensor array, as well as the effectiveness of the DOFC-enabled parallel interrogation, for PAT in vivo.

Discussion

In this work, a micro-ring sensor array containing 15 elements was demonstrated for PAT with DOFC-enabled parallel interrogation. In our framework, the limiting factor on the allowable sensor number is the bandwidth of the DOFC rather than the fabrication technique. DOFC-enabled parallel interrogation requires the resonant peaks of all micro-rings to be identifiable. Given the 40-GHz bandwidth of the DOFC and the 1.66-GHz separation of the resonant frequencies, at most 24 micro-rings can be accommodated theoretically. Given practical concerns such as crosstalk and the edge effect during the demodulation process, we chose to demonstrate 15 micro-rings so that each one could operate in the near optimum condition. Future works on increasing the sensor number can focus on either reducing the separation of the resonant frequencies or broadening the bandwidth of the DOFC. The prior one includes the efforts to further increase the quality factor of the micro-ring sensors. As for the latter one, one may consider integrating both digital and optical approaches to generate ultrafine OFC with broad bandwidth. With a greater number of micro-rings that can be interrogated parallelly, two-dimensional sensor arrays, including ring shape or bowl shape, can be realized and demonstrated for PAT, which is beneficial to the accommodation of various application scenarios.

In conclusion, we reported a micro-ring sensor array that contains 15 elements using chalcogenide glass. For such a new type of material that has rarely been explored in imaging and sensing, its large elastic-optical coefficients and low Young's modulus make it a promising candidate for optical ultrasound sensors. Specifically, the characterized parameters of this optical ultrasound array, including frequency bandwidth (175 MHz), NEP (2.2 mPaHz$^{-1/2}$), and acceptance angle (± 30 degrees), are comparable with those of state-of-the-art optical ultrasound sensors being reported [19, 27]. A comprehensive comparison is provided in Supplementary Note 5. We also developed an effective means of parallel interrogation to the micro-ring sensor array, which greatly simplifies the system setup and demodulation process by using only one source-detector pair. Demonstrations of PAT including imaging both fast-moving objects and live zebrafish at different growth stages were also provided. This work, which presents a chalcogenide-based micro-ring sensor array and its compatible DOFC-enabled parallel interrogation, is an important milestone in advancing optical ultrasound sensor arrays toward both preclinical and clinical applications in PAT.

Declarations

Acknowledgments

Competing interests

Additional information

Supplementary information.

References

1. A. Taruttis and V. Ntziachristos, "Advances in real-time multispectral optoacoustic imaging and its applications," Nature Photonics **9**, 219–227 (2015).

2. L. V. Wang and J. Yao, "A practical guide to photoacoustic tomography in the life sciences," Nature Methods **13**, 627 (2016).

3. L. Li, L. Zhu, C. Ma, L. Lin, J. Yao, L. Wang, K. Maslov, R. Zhang, W. Chen, J. Shi, and L. V. Wang, "Single-impulse panoramic photoacoustic computed tomography of small-animal whole-body dynamics at high spatiotemporal resolution," Nature Biomedical Engineering **1**, 0071 (2017).

4. X. Wang, Y. Pang, G. Ku, X. Xie, G. Stoica, and L. V. Wang, "Noninvasive laser-induced photoacoustic tomography for structural and functional in vivo imaging of the brain," Nature Biotechnology **21**, 803–806 (2003).

5. S. Na, J. J. Russin, L. Lin, X. Yuan, P. Hu, K. B. Jann, L. Yan, K. Maslov, J. Shi, D. J. Wang, C. Y. Liu, and L. V. Wang, "Massively parallel functional photoacoustic computed tomography of the human brain," Nature Biomedical Engineering (2021).

6. M. Toi, Y. Asao, Y. Matsumoto, H. Sekiguchi, A. Yoshikawa, M. Takada, M. Kataoka, T. Endo, N. Kawaguchi-Sakita, and M. Kawashima, "Visualization of tumor-related blood vessels in human breast by photoacoustic imaging system with a hemispherical detector array," Scientific Reports **7**, 41970 (2017).

7. L. Lin, P. Hu, J. Shi, C. M. Appleton, K. Maslov, L. Li, R. Zhang, and L. V. Wang, "Single-breath-hold photoacoustic computed tomography of the breast," Nature communications **9**, 1–9 (2018).

8. G. Wissmeyer, M. A. Pleitez, A. Rosenthal, and V. Ntziachristos, "Looking at sound: optoacoustics with all-optical ultrasound detection," Light: Science & Applications **7**, 53 (2018).

9. H. Lamela, D. Gallego, and A. Oraevsky, "Optoacoustic imaging using fiber-optic interferometric sensors," Opt. Lett. **34**, 3695–3697 (2009).

10. J. Bauer-Marschallinger, K. Felbermayer, and T. Berer, "All-optical photoacoustic projection imaging," Biomed. Opt. Express **8**, 3938–3951 (2017).

11. Y. Liang, L. Li, Q. Li, H. Liang, L. Jin, L. Wang, and B.-O. Guan, "Photoacoustic computed tomography by using a multi-angle scanning fiber-laser ultrasound sensor," Opt. Express **28**, 8744–8752 (2020).

12. A. Rosenthal, S. Kellnberger, D. Bozhko, A. Chekkoury, M. Omar, D. Razansky, and V. Ntziachristos, "Sensitive interferometric detection of ultrasound for minimally invasive clinical imaging applications," Laser & Photonics Reviews **8**, 450–457 (2014).

13. S. Ashkenazi, Y. Hou, T. Buma, and M. O'Donnell, "Optoacoustic imaging using thin polymer étalon," Applied Physics Letters **86**, 134102 (2005).

14. J. A. Guggenheim, J. Li, T. J. Allen, R. J. Colchester, S. Noimark, O. Ogunlade, I. P. Parkin, I. Papakonstantinou, A. E. Desjardins, E. Z. Zhang, and P. C. Beard, "Ultrasensitive plano-concave optical microresonators for ultrasound sensing," Nature Photonics **11**, 714–719 (2017).

15. Y. Chen, B. Chen, T. Yu, L. Yin, M. Sun, W. He, and C. Ma, "Photoacoustic Mouse Brain Imaging Using an Optical Fabry-Pérot Interferometric Ultrasound Sensor," Frontiers in Neuroscience **15**(2021).

16. R. Ansari, E. Z. Zhang, A. E. Desjardins, and P. C. Beard, "All-optical forward-viewing photoacoustic probe for high-resolution 3D endoscopy," Light: Science & Applications **7**, 75 (2018).

17. A. Rosenthal, D. Razansky, and V. Ntziachristos, "High-sensitivity compact ultrasonic detector based on a pi-phase-shifted fiber Bragg grating," Opt. Lett. **36**, 1833–1835 (2011).

18. A. Rosenthal, M. Omar, H. Estrada, S. Kellnberger, D. Razansky, and V. Ntziachristos, "Embedded ultrasound sensor in a silicon-on-insulator photonic platform," Applied Physics Letters **104**, 021116 (2014).

19. Y. Hazan, A. Levi, M. Nagli, and A. Rosenthal, "Silicon-photonics acoustic detector for optoacoustic micro-tomography," Nature Communications **13**, 1488 (2022).

20. R. Shnaiderman, G. Wissmeyer, O. Ülgen, Q. Mustafa, A. Chmyrov, and V. Ntziachristos, "A submicrometre silicon-on-insulator resonator for ultrasound detection," Nature **585**, 372–378 (2020).

21. R. Shnaiderman, Q. Mustafa, O. Ülgen, G. Wissmeyer, H. Estrada, D. Razansky, A. Chmyrov, and V. Ntziachristos, "Silicon-Photonics Point Sensor for High-Resolution Optoacoustic Imaging," Advanced Optical materials **9**, 2100256 (2021).

22. A. Maxwell, S. W. Huang, T. Ling, J. S. Kim, S. Ashkenazi, and L. J. Guo, "Polymer Microring Resonators for High-Frequency Ultrasound Detection and Imaging," IEEE Journal of Selected Topics in Quantum Electronics **14**, 191–197 (2008).

23. S.-W. Huang, S.-L. Chen, T. Ling, A. Maxwell, M. O'Donnell, L. J. Guo, and S. Ashkenazi, "Low-noise wideband ultrasound detection using polymer microring resonators," Applied Physics Letters **92**, 193509 (2008).

24. T. Ling, S.-L. Chen, and L. J. Guo, "High-sensitivity and wide-directivity ultrasound detection using high Q polymer microring resonators," Applied Physics Letters **98**, 204103 (2011).

25. H. Li, B. Dong, Z. Zhang, H. F. Zhang, and C. Sun, "A transparent broadband ultrasonic detector based on an optical micro-ring resonator for photoacoustic microscopy," Scientific Reports **4**, 4496 (2014).

26. C. Zhang, S. L. Chen, T. Ling, and L. J. Guo, "Review of Imprinted Polymer Microrings as Ultrasound Detectors: Design, Fabrication, and Characterization," IEEE Sensors Journal **15**, 3241–3248 (2015).

27. W. J. Westerveld, M. Mahmud-Ul-Hasan, R. Shnaiderman, V. Ntziachristos, X. Rottenberg, S. Severi, and V. Rochus, "Sensitive, small, broadband and scalable optomechanical ultrasound sensor in silicon photonics," Nature Photonics **15**, 341–345 (2021).

28. T. Ling, S.-L. Chen, and L. J. Guo, "Fabrication and characterization of High Q polymer micro-ring resonator and its application as a sensitive ultrasonic detector," Opt. Express **19**, 861–869 (2011).

29. Z. Xie, S.-L. Chen, T. Ling, L. J. Guo, P. L. Carson, and X. Wang, "Pure optical photoacoustic microscopy," Opt. Express **19**, 9027–9034 (2011).

30. C. Zhang, T. Ling, S.-L. Chen, and L. J. Guo, "Ultrabroad bandwidth and highly sensitive optical ultrasonic detector for photoacoustic imaging," Acs Photonics **1**, 1093–1098 (2014).

31. B. Dong, S. Chen, Z. Zhang, C. Sun, and H. F. Zhang, "Photoacoustic probe using a microring resonator ultrasonic sensor for endoscopic applications," Opt. Lett. **39**, 4372–4375 (2014).

32. B. Dong, H. Li, Z. Zhang, K. Zhang, S. Chen, C. Sun, and H. F. Zhang, "Isometric multimodal photoacoustic microscopy based on optically transparent micro-ring ultrasonic detection," Optica **2**, 169–176 (2015).

33. H. Li, B. Dong, X. Zhang, X. Shu, X. Chen, R. Hai, D. A. Czaplewski, H. F. Zhang, and C. Sun, "Disposable ultrasound-sensing chronic cranial window by soft nanoimprinting lithography," Nature Communications **10**, 4277 (2019).

34. Q. Rong, Y. Lee, Y. Tang, T. Vu, C. Taboada, W. Zheng, J. Xia, D. A. Czaplewski, H. F. Zhang, C. Sun, and J. Yao, "High-Frequency 3D Photoacoustic Computed Tomography Using an Optical Microring Resonator," BME Frontiers **2022**(2022).

35. J. D. Hamilton, T. Buma, M. Spisar, and M. O. Donnell, "High frequency optoacoustic arrays using etalon detection," IEEE Transactions on Ultrasonics, Ferroelectrics, and Frequency Control **47**, 160–169 (2000).

36. S.-W. Huang, Y. Hou, S. Ashkenazi, and M. O'Donnell, "High-resolution ultrasonic imaging using an etalon detector array," Applied Physics Letters **93**, 113501 (2008).

37. G. A. Cranch, P. J. Nash, and C. K. Kirkendall, "Large-scale remotely interrogated arrays of fiber-optic interferometric sensors for underwater acoustic applications," IEEE Sensors Journal **3**, 19–30 (2003).

38. H. Gabai, I. Steinberg, and A. Eyal, "Multiplexing of fiber-optic ultrasound sensors via swept frequency interferometry," Opt. Express **23**, 18915–18924 (2015).

39. Y. Hazan and A. Rosenthal, "Simultaneous multi-channel ultrasound detection via phase modulated pulse interferometry," Opt. Express **27**, 28844–28854 (2019).

40. Y. Bao, X. Yi, Z. Li, Q. Chen, J. Li, X. Fan, and X. Zhang, "A digitally generated ultrafine optical frequency comb for spectral measurements with 0.01-pm resolution and 0.7-µs response time," Light:

Science & Applications **4**, e300-e300 (2015).

41. J. Pan, B. Zhang, Z. Liu, J. Zhao, Y. Feng, L. Wan, and Z. Li, "Microbubble resonators combined with a digital optical frequency comb for high-precision air-coupled ultrasound detectors," Photon. Res. **8**, 303−310 (2020).

42. M. Xu and L. V. Wang, "Universal back-projection algorithm for photoacoustic computed tomography," Physical Review E **71**, 016706 (2005).

43. J. Zhu, M. Zohrabi, K. Bae, T. M. Horning, M. B. Grayson, W. Park, and J. T. Gopinath, "Nonlinear characterization of silica and chalcogenide microresonators," Optica **6**, 716−722 (2019).

44. B. Shen, H. Lin, S. Sharif Azadeh, J. Nojic, M. Kang, F. Merget, K. A. Richardson, J. Hu, and J. Witzens, "Reconfigurable Frequency-Selective Resonance Splitting in Chalcogenide Microring Resonators," ACS Photonics **7**, 499−511 (2020).

Figures
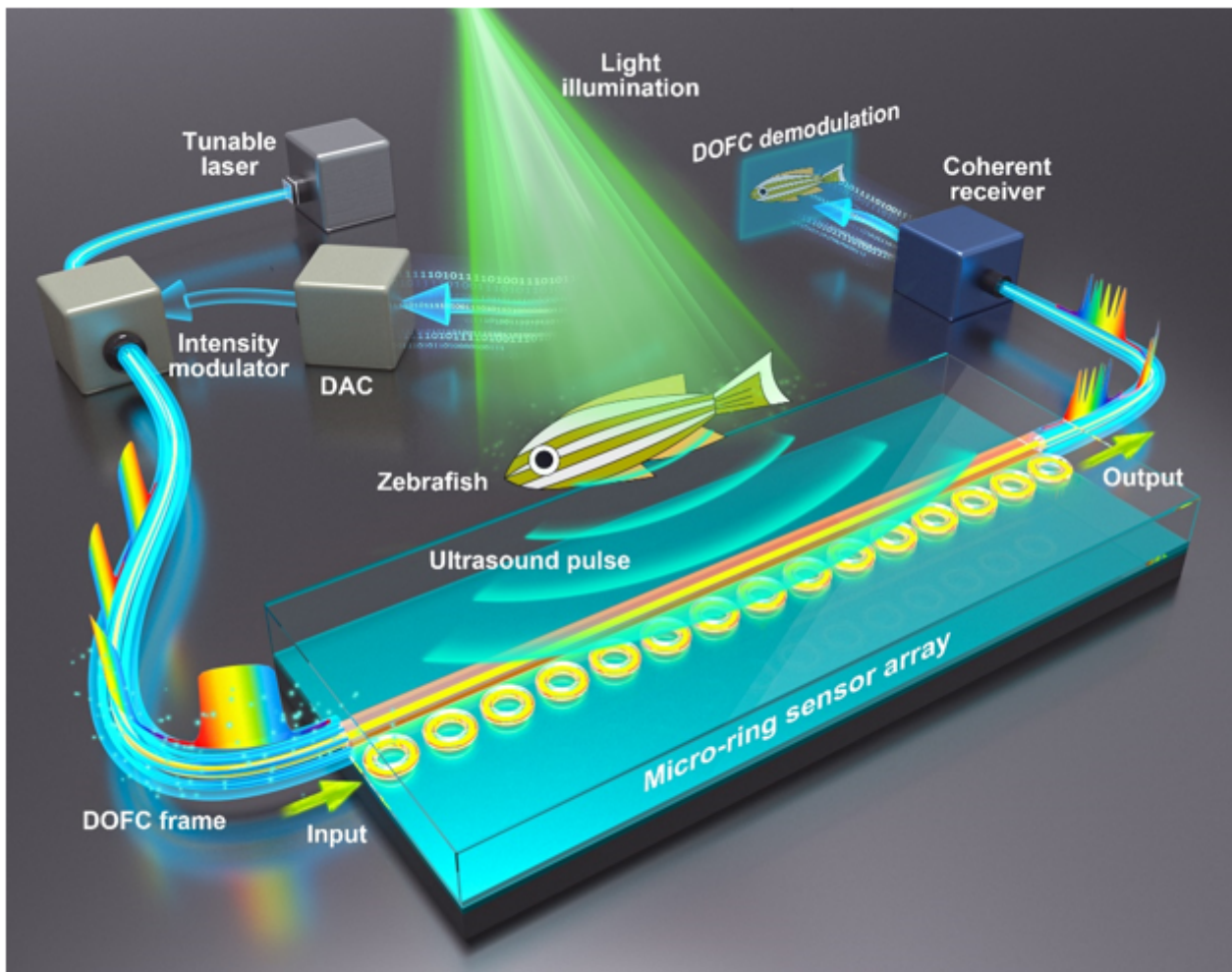
Figure 1

A schematic illustration of performing photoacoustic tomography (PAT) with the chalcogenide-based micro-ring sensor array. A digital optical frequency comb (DOFC) enabled parallel interrogation allows

acoustic signals at all micro-ring sensors to be acquired using only one light source and one photoreceiver in a one-time measurement. DAC: digital-to-analog converter.
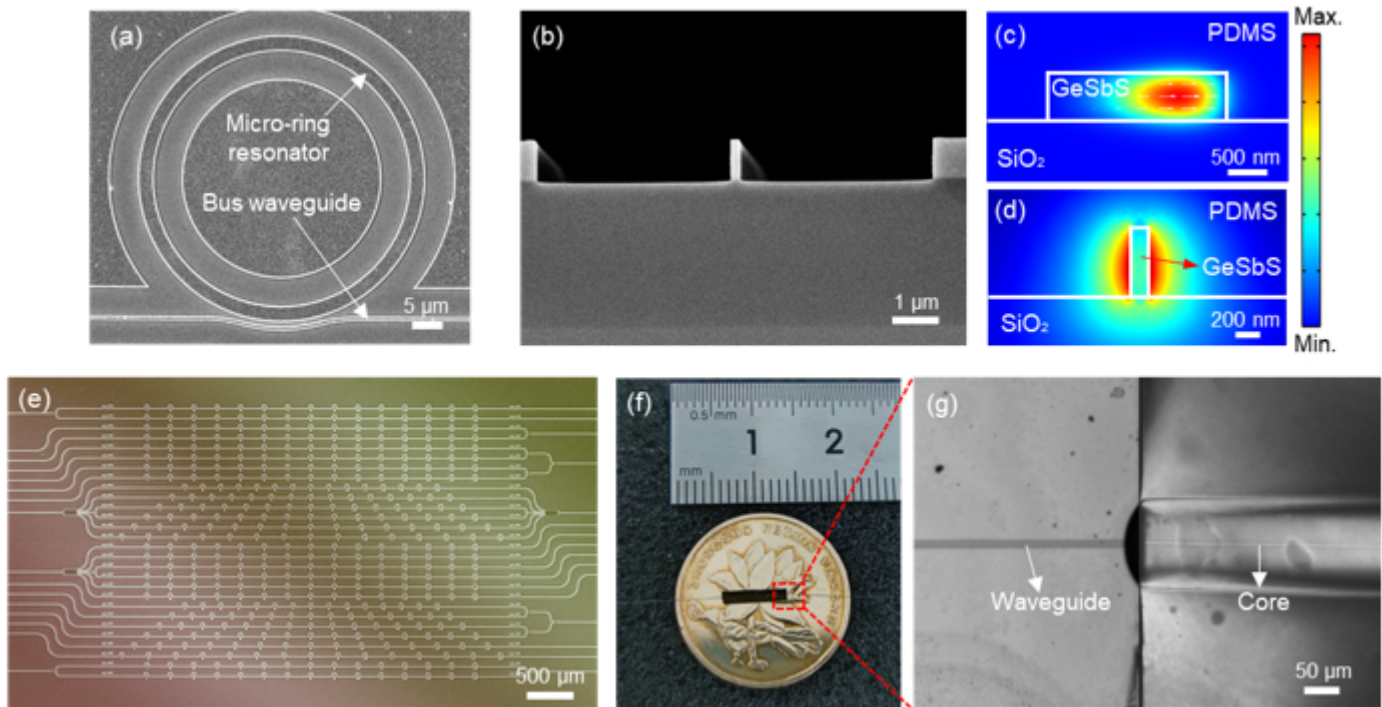

Figure 2

Structural description of the chalcogenide-based micro-ring sensor array. Each image has a different scale bar, which is provided in the lower right corner in white. (a) and (b) The scanning electron micrographs of a micro-ring sensor and a bus waveguide. (c) and (d) Numerical simulations of the mode profile, which are confined in the micro-ring sensor and the bus waveguide. (e) A microscope image of the chip, containing many micro-ring sensor arrays with different parameters. (f) A photo of the cleaved chip after encapsulation, which contains only one sensor array with a small footprint of about 6 mm × 2 mm. A nickel coin with a 2-cm diameter was placed underneath for comparison. (g) An enlarged view of the connection part between the bus waveguide and the single-mode optical fiber.
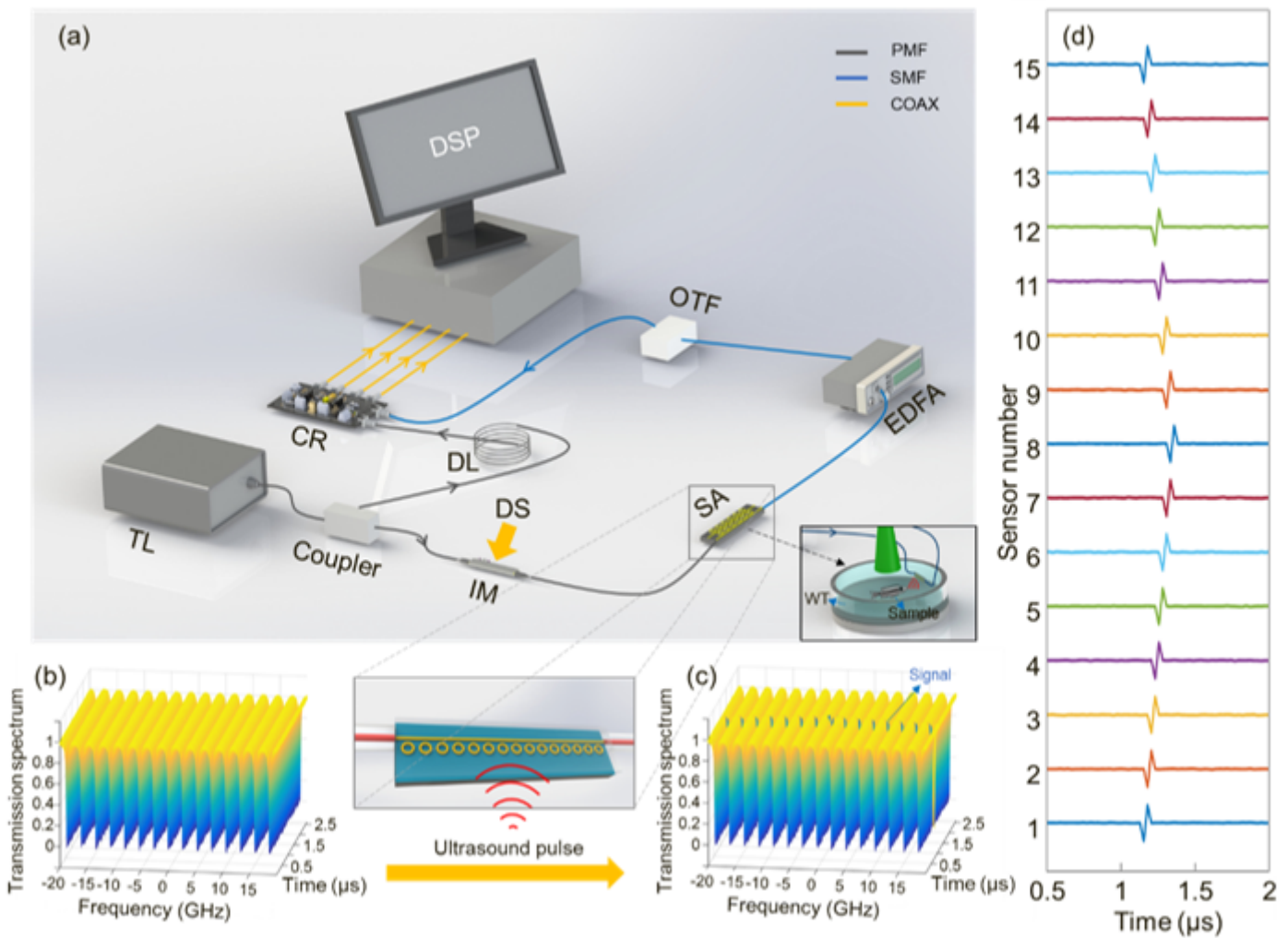
Figure 3

Experimental setup and operational principle to perform photoacoustic tomography using the chalcogenide-based micro-ring sensor array. (a) Experimental setup of the imaging system. The two insets show the generation and receiving processes of the PA signal. TL, tunable laser; IM, intensity modulator; DS: digital signal; SA: sensor array; WT: water tank; EDFA: erbium-doped fiber amplifier; OTF: optical tunable filter; DL: optical delay line; CR: coherent receiver; DSP: digital signal processing; PMF: polarization maintaining fiber; SMF: single mode fiber; COAX: coaxial cable. (b) The measured transmission spectrum of the sensor array as a function of time in the null case. (c) The measured transmission spectrum of the sensor array when ultrasound is present to modulate the sensor array. (d) The reconstructed ultrasound signal as a function of time for each micro-ring sensor.
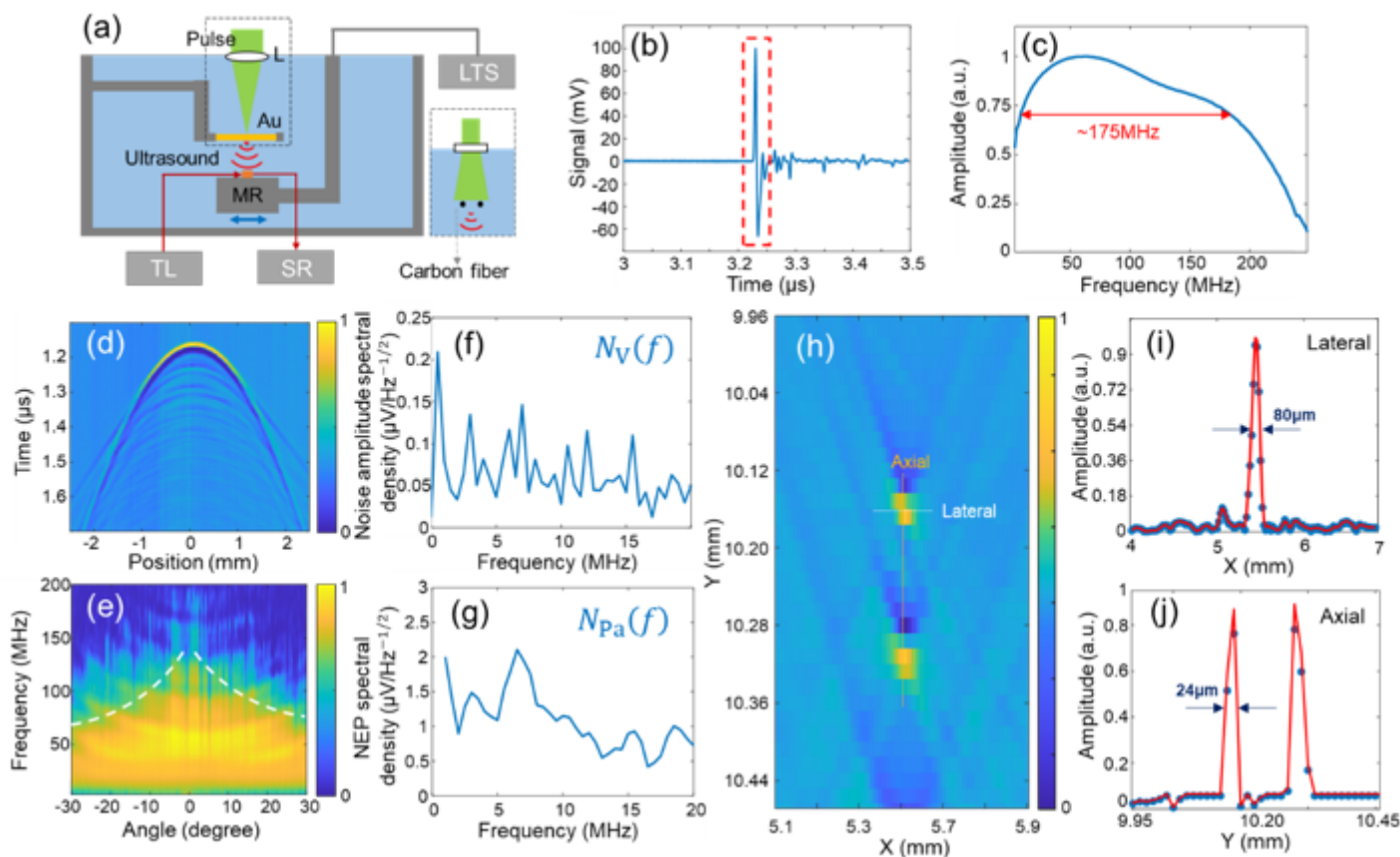
Figure 4

Characterization of the micro-ring ultrasound sensor. (a) Schematic illustration of the characterization system that focuses pulsed light onto a golden thin fil to generate a point-like ultrasound source. L: lens; TL: tunable laser; SR: signal receiver; MR: micro-ring. LTS: linear translational stage. (b) The measured PA signal as a function of time. A time window (red dashed box) was implemented to keep only the first arriving signals while excluding the following ones due to multiple reflections. (c) The frequency response of the micro-ring sensor. The center frequency is around 60 MHz, and the -6 dB bandwidth is about 175 MHz. (d) Amplitude map of the measured PA signal as a function of time and translational distance. (e) Frequency response as a function of the acceptance angle. Two -3 dB lines are also provided in white. (f) Noise amplitude spectral density of the micro-ring sensor. (g) Noise-equivalent-pressure (NEP) spectral density of the micro-ring sensor. (h) Reconstructed images of the cross-section of carbon fibers buried inside the agar. (i) One-dimensional profile along the lateral direction, suggesting a lateral resolution of 80 μm. (g) One-dimensional profile along the axial direction, suggesting an axial resolution of 24 μm.
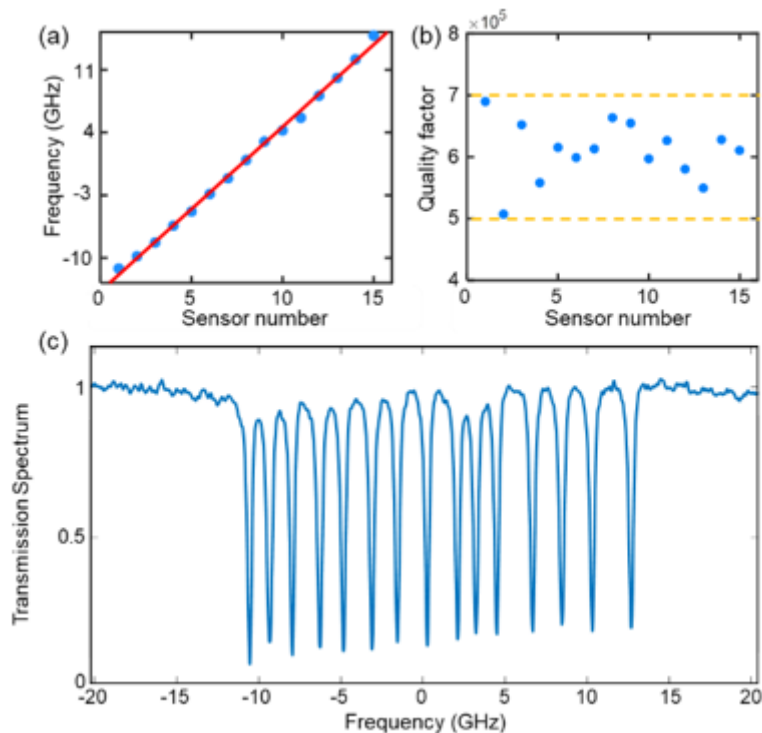
Figure 5

Frequency tuning for the micro-ring sensor array with 15 micro-rings. (a) Resonant frequencies of the micro-ring sensors after frequency tuning, which are ordered and equally spaced with respect to their labeling. (b) The quality factors of these micro-ring sensors after frequency tuning, exhibiting good consistency. (c) A typical transmission spectrum of the micro-ring sensor array after frequency tuning, exhibiting 15 discrete resonant dips.
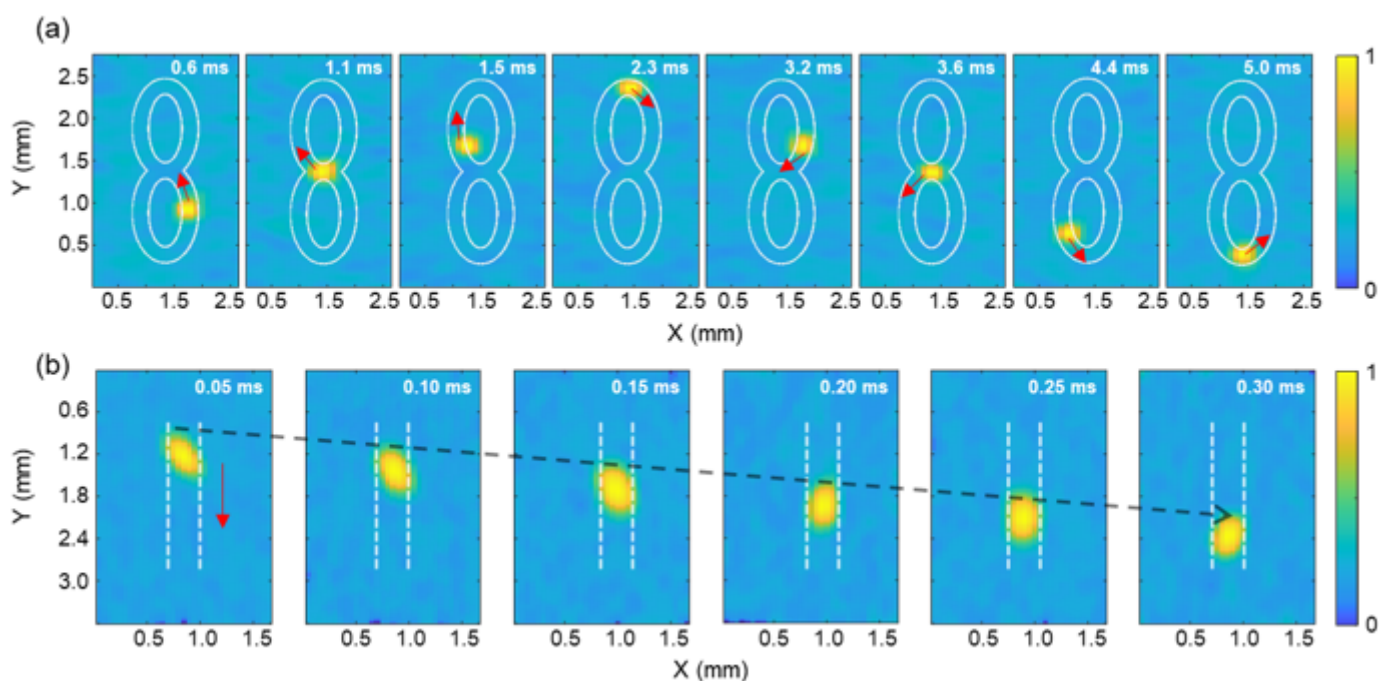
Figure 6

Experimental results of imaging fast-moving objects using the micro-ring sensor array with parallel interrogation. (a) Representative images of a fast-moving hot spot along a trajectory of '8' shape. (b) Imaging results for a polystyrene microsphere moving in motion.
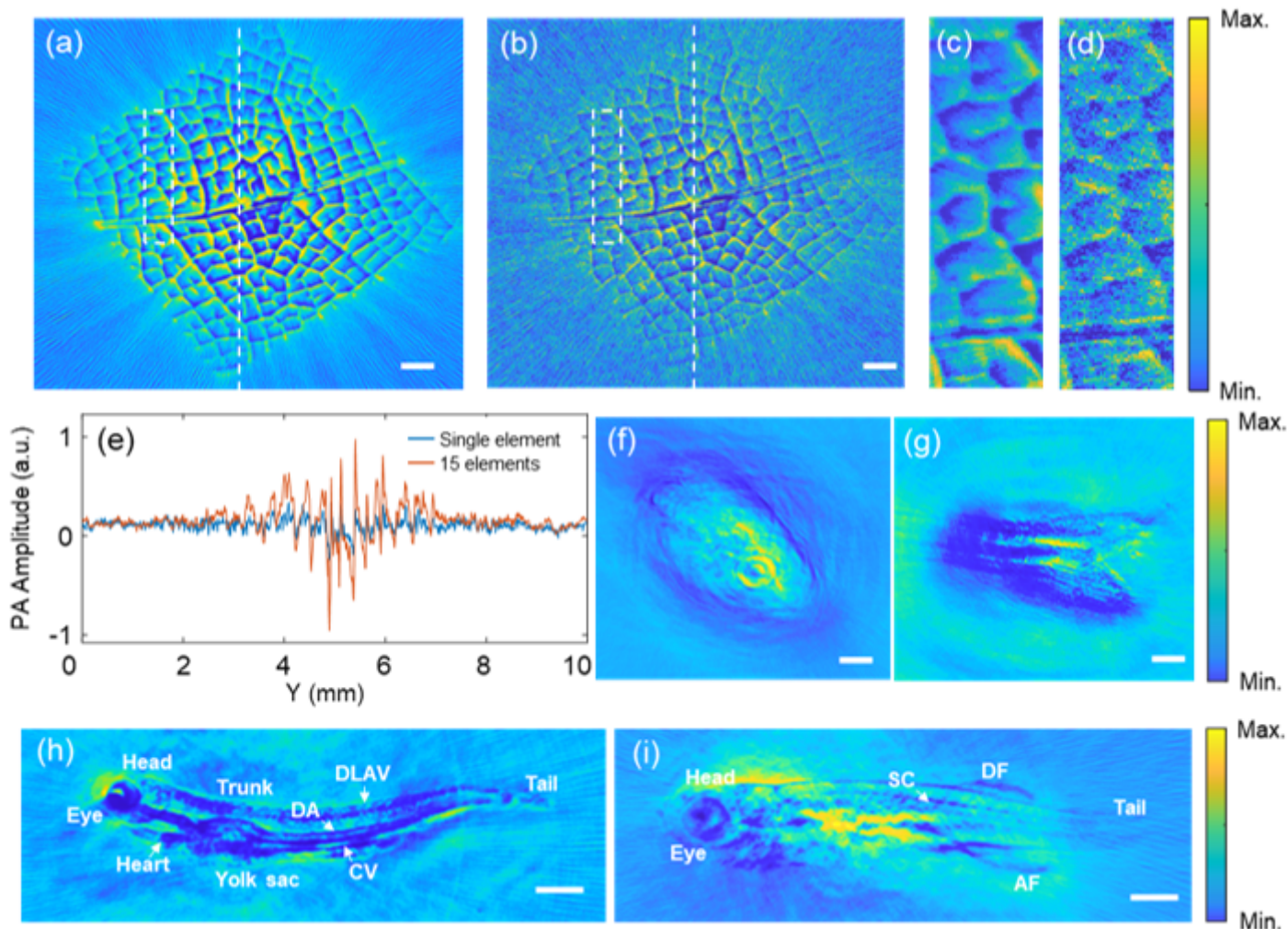

Figure 7

Experimental results of imaging biological sample using the micro-ring sensor array with parallel interrogation. Scale bars: 1 mm. (a) Imaging result of a piece of leaf buried inside 5-mm thick tissue-mimicking phantoms using the micro-ring sensor array. (b) imaging result of the same leaf using only one micro-ring sensor. (c) and (d) Enlarged view of the area enclosed in white dashed boxes in (a) and (b). (e) One-dimensional profiles along the white lines in the reconstructed images in (a) and (b) are plotted in red and blue, respectively. (f) Reconstructed image of the head of a 3-month-old adult zebrafish using the micro-ring sensor array. (g) Reconstructed image of the tail of a 3-month-old adult zebrafish using the micro-ring sensor array, (h) Whole-body imaging of a zebrafish 7 days post-fertilization using the micro-ring sensor array. DA: dorsal aorta; CV: cardinal vein; DLAV: dorsal longitudinal anastomotic

vessel. (i) Whole-body imaging of a zebrafish 20 days post-fertilization using the micro-ring sensor array. SC: spinal column DF: dorsal fin; AF: anal fin.

Supplementary Files

This is a list of supplementary files associated with this preprint. Click to download.

- 20220815Supplementaryv9.docx